RPE | Radiation Physics & Engineering
A Peer-Reviewed Journal
Published by K.N. Toosi University of Technology
http://rpe.kntu.ac.ir
Research Article

Radiation Physics and Engineering 2027; ?(?):?–?

Linking cellular dosimetry and nanoscale DNA damage of key accident radionuclides using MCNPX and Geant4-DNA

Kambiz Kangarlou[a], Bahman Jalali Kondori[b], Mohammad Taghi Holisaz[c], Parisa Taghipour Niyar[a], Masoumeh Soleimaninia[a], Amir Moslehi[a], Armin Mosayebi[a], Seyed Pezhman Shirmardi[a,*], Seyed Mohamad Mazidi[a]

[a] *Radiation Application Research School, Nuclear Science and Technology Research Institute, Tehran, Iran*
[b] *Department of Anatomical Science, Faculty of Medicine, Baqiyatallah University of Medicine Science, Tehran, Iran*
[c] *Department of physical medicine and Rehabilitation, Faculty of Medicine, Baqiyatallah University of Medicine Science, Tehran, Iran*

Rejected

HIGHLIGHTS

- Cellular dose depends on radionuclide, radiation quality, and source location.
- Multicellular simulations reveal significant cross-doses in neighboring cells.
- Lower-energy betas cause higher DNA damage due to increased LET.
- The MCNPX and Geant4-DNA framework improves radiation risk assessment.

ABSTRACT

Radionuclides released during nuclear accidents can induce significant biological effects through both external and internal exposure. Understanding the relationship between radionuclide characteristics, cellular dose distribution, and DNA damage is essential for accurate radiation risk assessment. In this study, the radiobiological effects of three important radionuclides Cs-137, I-131, and Sr-90 were investigated using a multiscale Monte Carlo approach. Cellular dosimetry calculations were performed with MCNPX to evaluate energy deposition of beta particles and gamma rays within the cell membrane, cytoplasm, and nucleus. Concurrently, Geant4-DNA simulations were used to quantify radiation-induced DNA strand breaks. The model was extended from a single-cell to a multicellular geometry to assess both self-dose and cross-dose. The results demonstrated that absorbed dose distribution strongly depends on radionuclide type, radiation quality, and source location. For an intracellular source, the highest doses were observed in the compartment containing the source, whereas for an extracellular source the cell membrane received the largest dose. Multicellular simulations showed that although the source containing cell absorbed the highest dose, neighboring cells also received measurable doses. At the molecular level, lower-energy beta particles produced higher SSB and DSB yields due to their elevated linear energy transfer and more localized energy deposition, while higher-energy beta particles resulted in lower damage induction. The calculated SSB and DSB yields ($Gy^{-1}.Gbp^{-1}$) were as follows:

- Cs-137 γ (662 keV): SSB = 264.1 ± 1.3, DSB = 3.5 ± 0.1
- I-131 γ: SSB = 278.9 ± 1.1, DSB = 3.5 ± 0.1
- I-131 β: SSB = 88.5 ± 0.1, DSB = 2.4 ± 0.2
- Sr-90 β (546 keV): SSB = 280.3 ± 16.7, DSB = 3.5 ± 1.9
- Sr-90 β (2.38 MeV): SSB = 3.5 ± 1.9, DSB = 0.085 ± 0.03

The combined MCNPXGeant4-DNA framework provides a multiscale description of energy deposition and DNA damage that can support a more detailed radiobiological interpretation of accidental radionuclide exposures.

KEYWORDS

Monte Carlo simulation
MCNPX
Geant4-DNA
Cellular dosimetry
DNA damage
Single-strand break
Double-strand break

HISTORY

Received:
Revised:
Accepted:
Published:

*Corresponding author: p_shirmardi@aut.ac.ir

https://doi.org/

1 Introduction

The release of radioactive materials into the environment can have significant biological and environmental consequences for humans, animals, plants, and ecosystems. Major nuclear events throughout history, including the explosion at the Chernobyl Nuclear Power Plant in the former Soviet Union (Ukraine) in 1986, the Fukushima Daiichi Nuclear Power Plant accident in Japan in 2011, and the use of atomic weapons against the cities of Hiroshima and Nagasaki in 1945, have highlighted the necessity of carefully investigating the hazards associated with the release of radioactive materials. These events have prompted researchers to extensively study the effects of technical failures, human errors, natural disasters, and wars, all of which can lead to the release and dispersion of radionuclides into the environment. The aim of these investigations is to understand the patterns of radionuclide transport and dispersion in the environment, examine the pathways through which they enter the human body, and assess their potential health and environmental consequences, thereby enabling the development of preventive and management strategies to minimize the risks associated with nuclear activities (Ory et al., 2021).

In a nuclear accident, the release of radioactive materials generally occurs as a result of damage to systems designed to contain nuclear materials, such as fuel cladding, the reactor building, or cooling systems. As a result of increased temperature or pressure, or structural damage, fission products and other radionuclides may escape from their containment and enter the environment. These materials can be transported through the air, water, and soil, leading to environmental contamination. Individuals present in the affected area may be exposed to radiation through external irradiation from radioactive sources present in the environment or through internal contamination resulting from the inhalation, ingestion, or entry of radioactive materials into the body. The severity of the health consequences depends on factors such as the type of radioactive material, the amount released, the route of entry into the body, the duration of exposure, and the dose received (IAEA, nd; Mészáros et al., 2016).

The type and magnitude of radiation exposure following a nuclear accident depend largely on the radionuclides released and their physical and biological characteristics. Important factors include radioactive half-life, decay mode, energy of emitted radiation, chemical behavior, and the ability of each radionuclide to accumulate in specific organs or tissues. For example, some radionuclides mainly contribute to external exposure due to their penetrating gamma emissions, whereas others may pose significant internal exposure risks because of their biological uptake and retention within the body (United Nations Scientific Committee on the Effects of Atomic Radiation, 2021).

Iodine-131 (I-131) and cesium-137 (Cs-137) are among the most significant radionuclides released during nuclear reactor accidents, particularly during the Chernobyl and Fukushima Daiichi accidents. Iodine-131 is a short-lived radionuclide with a half-life of approximately 8 days and undergoes beta decay accompanied by gamma emissions. Due to its chemical similarity to stable iodine, it can accumulate in the thyroid gland, resulting in localized radiation exposure and an increased risk of thyroid-related health effects. Cesium-137, with a half-life of approximately 30 years, is a major environmental contaminant due to its long persistence in ecosystems. It undergoes beta decay to metastable barium-137m, followed by the emission of a characteristic 662 keV gamma photon, making it an important contributor to both external and internal radiation exposure (Steinhauser et al., 2014; Chino et al., 2011; Wai et al., 2020). In addition to gamma-emitting radionuclides, pure beta emitters can represent important internal radiation hazards. Strontium-90 (Sr-90) is a beta-emitting fission product with a half-life of approximately 29 years. Due to its chemical similarity to calcium, strontium can accumulate in bone tissue, where its continuous beta emissions may irradiate surrounding cells and contribute to long-term biological effects (Paquet et al., 2017).

In the present study, I-131, Cs-137, and Sr-90 were selected for investigation. The selection of I-131, Cs-137, and Sr-90 in the present study was based on their radiological significance, distinct biokinetic behaviors, and their frequent occurrence following nuclear accidents. These radionuclides represent different pathways of internal contamination and target different organs due to their chemical properties. I-131 is readily absorbed through inhalation or ingestion and preferentially accumulates in the thyroid gland because of its chemical similarity to stable iodine. Cs-137, which behaves similarly to potassium, is widely distributed throughout soft tissues after entering the body, primarily through contaminated food, water, or inhalation. In contrast, Sr-90 exhibits chemical properties similar to calcium and is preferentially incorporated into bone tissue following ingestion, where it may remain for extended periods and continuously irradiate surrounding cells. Consequently, these radionuclides provide representative models for investigating of radiation effects in different biological targets and exposure scenarios (Higley, 2006; UNSCEAR, 2021).

Following the entry of ionizing radiation into the body, biological damage occurs through two main pathways: the direct and indirect effects of radiation. In the direct effect, radiation energy is transferred directly to vital cellular molecules, particularly DNA, causing ionization and structural alterations. In the indirect effect, radiation initially interacts with water molecules present in cells, which constitute a major component of the body, resulting in the radiolysis of water and the formation of reactive oxygen species (ROS), such as hydroxyl radicals ($^{\bullet}$OH), as well as other free radicals. These highly reactive molecules can damage cellular components, including DNA, proteins, and cell membranes. Since water is the most abundant molecule in biological tissues, the indirect pathway is considered one of the most important mechanisms responsible for radiation-induced damage (IAEA, 2015).

Radiation-induced DNA damage includes single-strand breaks (SSBs) and double-strand breaks (DSBs) in the DNA molecule. Among these types of damage, DNA

Uncorrected Proof

double-strand breaks are of particular importance because, if repaired inaccurately, they can lead to genetic mutations, chromosomal instability, and ultimately an increased probability of cellular transformation and carcinogenesis. Cells possess DNA repair systems, such as non-homologous end joining (NHEJ) and homologous recombination (HR), which attempt to repair this damage; however, some lesions may be repaired incorrectly or may remain unrepaired. Consequently, the fate of a cell following irradiation may involve complete repair, cell death, or the persistence of mutations that may contribute to the development of diseases such as cancer over the long term (National Research Council, 2006).

The biological effects induced by ionizing radiation are strongly influenced by the physical characteristics of the emitted radiation, including particle type, energy, linear energy transfer (LET), and the spatial distribution of energy deposition within tissues. Different radionuclides can emit alpha and beta particles, and also gamma photons, resulting in distinct patterns of radiation interaction with biological matter. Beta particles have lower LET values but can cause significant cellular damage through both direct ionization and the generation of reactive oxygen species. Gamma photons, as low-LET electromagnetic radiation, have greater penetration depth and can contribute to whole-body external exposure, while also inducing indirect DNA damage through water radiolysis (Nikjoo et al., 1997; Hada and Georgakilas, 2008).

Considering the different physical properties, biological behaviors, and radiation qualities of these radionuclides, understanding their interactions with biological systems is essential for evaluating radiation risks. Investigation of DNA damage induced by alpha, beta, and gamma ray from different radionuclides provides valuable insight into the mechanisms underlying radiation-induced biological effects and supports the development of improved radiation protection strategies, dosimetric approaches, and risk assessment models.

Because experimental investigation of radiation interactions at the cellular and subcellular levels is often limited by technical, ethical, and dosimetric constraints, Monte Carlo simulation has become an indispensable tool in radiation physics and radiobiology. Monte Carlo transport codes enable detailed modeling of radiation interactions over a wide range of spatial scales, from whole tissues to individual cellular compartments and even DNA structures. Among these computational tools, the Monte Carlo N-Particle (MCNP) code has been extensively employed for accurate particle transport and energy deposition calculations in complex geometries, whereas the Geant4-DNA extension provides track-structure simulations capable of modeling physical and physicochemical interactions of charged particles with biological matter down to the nanometer scale. The combination of these simulation approaches enables comprehensive evaluation of radiation transport, absorbed dose distribution, and radiation-induced DNA damage, thereby providing valuable insight into the mechanisms underlying the biological effects of ionizing radiation (Sadremomtaz and Masoumi, 2018; El Naqa et al., 2012; Kyriakou et al., 2021; Sakata et al., 2020; de la Fuente Rosales et al., 2018; Cai et al., 2010).

The aim of the present study was to investigate the biological effects of three radionuclides frequently encountered in nuclear accidents and radiation applications, namely I-131, Cs-137, and Sr-90, using Monte Carlo simulations. MCNP was employed to evaluate radiation transport and absorbed dose distributions within different cellular compartments, including the cell membrane, cytoplasm, and nucleus, while Geant4-DNA was used to investigate radiation-induced DNA damage at the molecular level, with particular emphasis on single-strand and double-strand DNA breaks. By integrating cellular dosimetry with nanoscale DNA damage simulations, this study aims to compare the radiobiological characteristics of beta-, and gamma-emitting radionuclides and to provide a more comprehensive understanding of the relationship between radiation quality, energy deposition, and biological effectiveness. The findings of this work may contribute to improved radiation risk assessment, optimization of radiation protection strategies, and preparedness for accidental radionuclide releases. To the best of our knowledge, limited studies have combined Monte Carlo simulations to investigate radiation transport and DNA damage induced by multiple beta, and gamma-emitting radionuclides within a unified computational framework (Jolly and Fielding, 2025).

2 Material and methods

To investigate the biological effects of I-131, Cs-137, and Sr-90, Monte Carlo simulations were performed. This methodology integrates cellular-level dosimetry using the MCNPX code, with nanoscale track-structure simulations conducted via the Geant4-DNA toolkit to quantify radiation-induced DNA damage. To establish the physical basis of the radiation sources used in the simulations, the decay schemes, principal decay products, and associated radiation emissions of the investigated radionuclides are presented below.

2.1 Decay scheme of the radionuclides

The decay schemes of Cs-137, I-131, and Sr-90 are shown in Figs. 1 to 3. A brief description of these radionuclides will be presented in the following.

Cs-137 is one of the major fission products of U-235 and is commonly released into the environment following nuclear power plant accidents. It undergoes decay to Ba-137, predominantly populating the metastable state Ba, which subsequently de-excites by emitting a characteristic 662 keV gamma ray. Consequently, Cs-137 acts as both a beta and a relatively high-energy gamma emitter, contributing to both internal and external radiation exposure. Figure 1 illustrates the decay scheme of Cs-137 (Leblond, 2024).

Originally, I-131 was produced by bombarding stable tellurium with deuterons. Nowadays, I-131 is obtained primarily as a reactor by-product from fission of U-235 atoms. Both methods produce Te-131, which decays to

Uncorrected Proof

I-131 according to the Fig. 2. Half of the amount of the radioactive iodine will decay within 8 days. The main decay product is Xe-131 (Kocher, 1980).

The transition energy between I-131 and the 131Xe ground state is 971 keV. The first emission product is an electron with a range in energy between 250 keV- 800 keV. Electrons in this energy range usually travel less than a mm before depositing their energy and causing an ionization event. This means that most of the damage from the electrons produced from the decay of I-131 occurs in the cells in which the I-131 is concentrated. The second product of I-131 is a moderate energy photon 364 keV.

Figure 3 shows the decay scheme of Sr-90, which emits beta-rays without emitting a gamma-ray. Owing to the high-energy beta particles emitted by Y-90, the Sr-90 - Y-90 system is an important source of beta and can deliver substantial localized radiation doses following internal contamination (Nam et al., 2017).

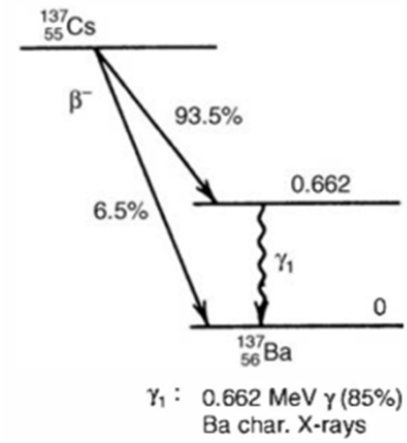

Figure 1: Decay scheme of Cs-137.

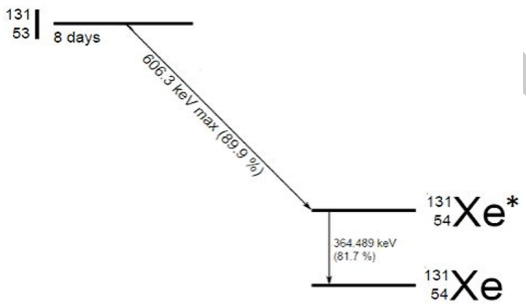

Figure 2: Decay scheme of I-131.

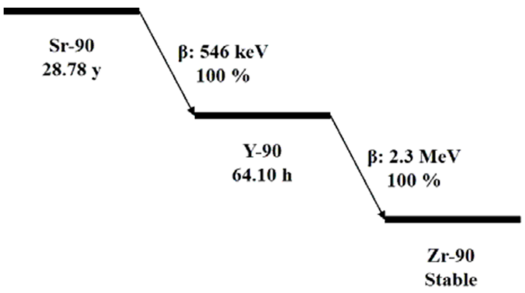

Figure 3: Decay scheme of Sr-90.

2.2 *Cell model and Calculation of cellular dose using MCNPX*

The nucleus is the most crucial part of the cell, primarily made of water and protein with a density of 1.2 g.cm^{-3}. The other components are the cytoplasm, which is made of with a density of 1.06 g.cm^{-3}, and the membrane which has a density of 1.1 g.cm^{-3}. A single cell, as depicted in Fig. 4, was assumed to be composed of three concentric spheres with radii of 5 μm, 10 μm and 10.01 μm for the nucleus, cytoplasm, and membrane, respectively.

In this study, the MCNP radiation transport code was employed to simulate the transport of beta particles and also gamma rays emitted by I-131, Cs-137, and Sr-90 radionuclides. In the first step, a single-cell model according to Fig. 4 containing the radionuclide source was developed to evaluate the energy deposition and absorbed dose within the different parts of the cell. In this case, the point sources were evaluated at two distinct positions: (1) intracellularly, at the center of the cytoplasm, and (2) extracellularly, outside the cell at a distance of 0.1 cm. The medium surrounding the cell was assumed to be air. It should also be noted that all calculations were performed using the maximum beta-particle energy in each spectrum, while taking the branching ratio into account.

Subsequently, the model was extended to include several cells surrounding the source-containing cell to better reflect realistic biological conditions and to investigate the spatial distribution of radiation dose in adjacent cells. This approach allows for the determination of both the self-dose delivered to the source-containing cell and the cross-dose deposited in surrounding cells due to radiation transport. The schematic representation of the multicellular configuration used for dose assessment is shown in Fig. 5, where the source-containing cell is located at the center and surrounded by neighboring cells arranged in two concentric rings to evaluate the spatial distribution of beta radiation dose.

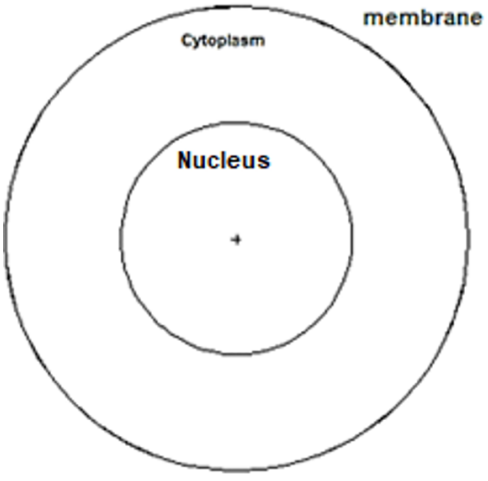

Figure 4: Simulation geometry in MCNPX used to estimate the dose deposited in different cellular compartments; 1 (nucleus), 2 (cytoplasm), 3 (cell membrane). The cell is modeled as three concentric spheres with radii of 5 μm, 10 μm and 10.01 μm for the nucleus, cytoplasm, and membrane, respectively.

Uncorrected Proof

Table 1: Characteristics of the atoms that make up the simulated DNA di-nucleosome with a total of 14,221 atoms.

Color	Atom	Number of Atoms	Radius (nm)	Volume (nm)
Gray	Carbon (C)	6788	0.170	0.02058
Red	Oxygen (O)	4160	0.152	0.01471
Dark Blue	Nitrogen (N)	2581	0.155	0.01560
Orange	Phosphorus (P)	692	0.180	0.02443

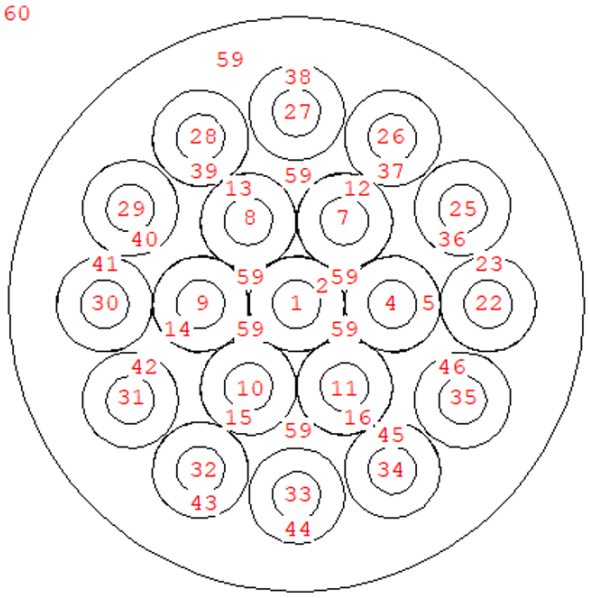

Figure 5: Schematic configuration of the cell array used for dose assessment. The source is located at the center with surrounding cells arranged in two concentric rings to evaluate the beta dose distribution.

It is worth mentioning that energy deposition tallies for photons and electrons (F6 and *F8) were employed to record the absorbed dose per primary particle in the nucleus, cytoplasm, and membrane. For each simulation, approximately 10^8 to 10^9 particles were simulated to ensure a relative error of less than 1% for all energy deposition results.

2.3 Quantifying DNA damage

While cellular-level dosimetry provides a macro-scale understanding of energy deposition in the cell, evaluating the actual radiobiological risk requires an analysis of damage at the molecular level. This section bridges the gap between dose assessment and biological response by employing the Geant4-DNA toolkit to simulate ionizing track structures. By focusing on the nanoscale interaction between radiation and DNA, we aim to quantify the induction of Single-Strand Breaks (SSBs) and Double-Strand Breaks (DSBs), thereby elucidating the ultimate biological impact of the investigated radionuclides.

To achieve this, the calculations were performed using the Geant4 simulation toolkit (Agostinelli et al., 2003), version 11.1.0. The DNA macromolecular structure was obtained from the Protein Data Bank (PDB) and imported into Geant4 as a separate file named "1ZBB.PDB", representing a di-nucleosome. This atomic model contains 347 DNA base pairs arranged in two chains, with a total of 14,221 atoms. The structure has dimensions of 25.1 nm × 15 nm × 9.5 nm and was enclosed within a water cube. The mass of the di-nucleosome is 215,935 Da, corresponding to 3.59×10^{-22} kg. A schematic view of the simulated DNA macromolecule is shown in Fig. 6. In this figure, each colored sphere represents an atom; the characteristics of the colored spheres and their corresponding atoms are presented in Table 1. All atoms were assumed to be composed of water.

For the simulation of radiation-induced DNA damage, the Geant4-DNA physics model was employed to transport electrons down to an energy threshold of 5 eV. The radiation source was defined as a cubic volume with dimensions identical to those of the water box surrounding the DNA macromolecule, and particles were emitted toward the DNA with a cosine angular distribution.

For I-131, beta particles with a maximum energy of 606 keV and gamma rays with an energy of 364 keV were considered. Similar to the case of Cs-137, the probability of direct interaction of gamma photons with the DNA target was negligible; therefore, the equilibrium spectrum of secondary electrons generated in water was used instead. This spectrum was calculated using the MCNP code by simulating a 364 keV point gamma source in a water phantom and determining the secondary electron fluence in a sensitive volume using the F4 tally. The resulting electron spectrum is presented in Fig. 7-a.

For Cs-137, direct interaction of the 662 keV gamma photons with the DNA structure is highly unlikely due to the nanometric dimensions of the simulated target. Therefore, the equilibrium spectrum of secondary electrons generated by these photons in water was used as the irradiation source. The resulting secondary electron spectrum is shown in Fig. 7-b (Semsarha et al., 2014).

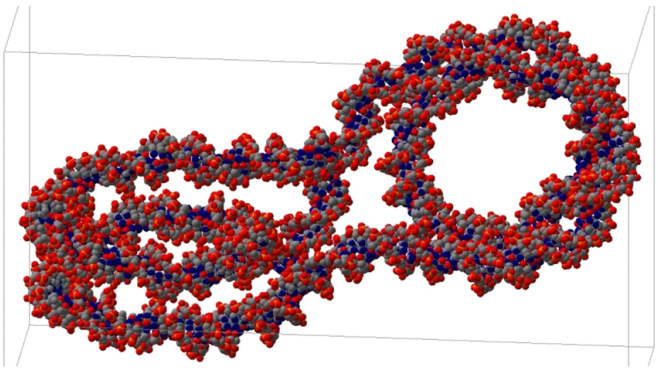

Figure 6: Schematic representation of the DNA di-nucleosome structure retrieved from the PDB (ID: 1ZBB).

Uncorrected Proof

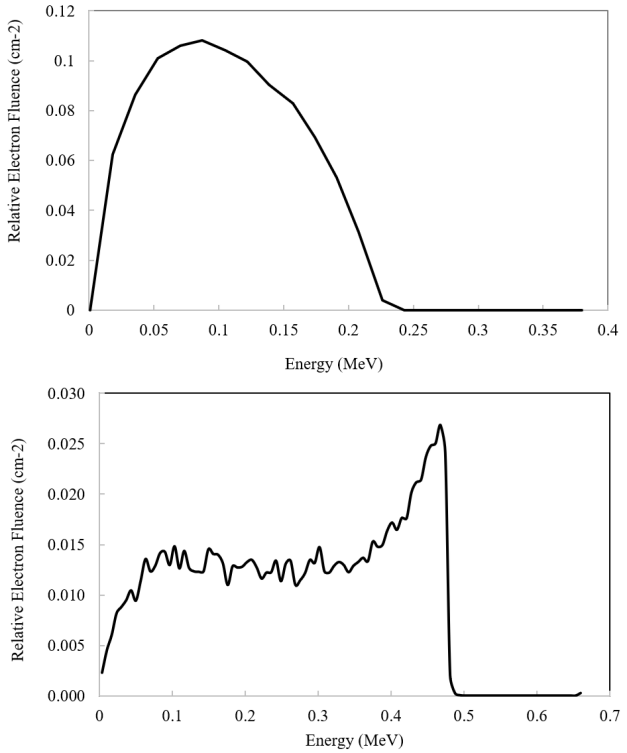

Figure 7: a) Energy spectrum of secondary electrons generated by I-131. b) Energy spectrum of secondary electrons generated by Cs-137 (Semsarha et al., 2014).

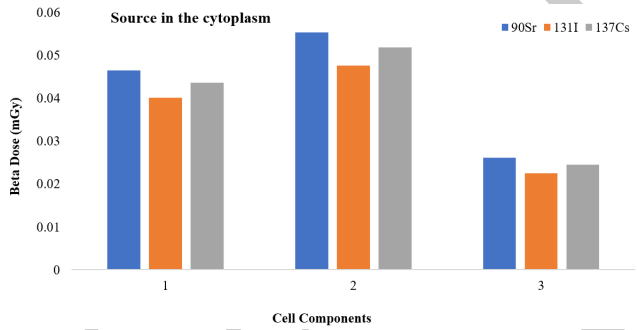

Figure 8: Beta dose deposition within the cellular components (1: Nucleus, 2: Cytoplasm, 3: Membrane) for Sr-90, I-131, and Cs-137 sources.

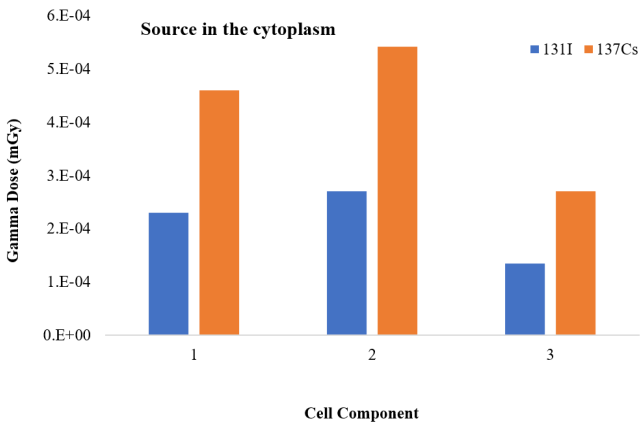

Figure 9: Gamma dose deposition within the cellular components (1: Nucleus, 2: Cytoplasm, 3: Membrane) for Sr-90, I-131, and Cs-137 sources.

For Sr-90, the emitted beta particles with maximum energies of 546 keV and 2.28 MeV, respectively, were directly simulated. Both beta-emission branches were considered with branching ratios equal to unity.

In the next step, the sugarphosphate groups in both DNA strands are treated as sensitive volumes, and the energy deposited in them is calculated. When the deposited energy in a sugarphosphate group is greater than or equal to 10.79 eV, a single-strand break (SSB) is recorded (Semsarha et al., 2014). If two single-strand breaks (SSBs) occur simultaneously on both DNA strands within a distance of 10 base pairs, it is considered as a double-strand break (DSB).

The yields of SSB or DSB is calculated using Eq. (1):

$$Y_{SSB/DSB} = \frac{10^9}{347} \times \frac{N_{SSB/DSB}}{D} \quad (1)$$

where $N_{SSB/DSB}$ represents the number of single- or double-strand breaks, and D is the absorbed dose in the macromolecule in Gy. Equation (1) provides the strand-break yield per unit absorbed dose per 1 Gbp (10^9 base pairs). It is worth noting that the number of incident particles was set to 1×10^8 in order to ensure that the relative statistical error (Type A (Taylor, 2009)) of the absorbed dose was less than 1%.

3 Results and discussion

3.1 Results of MCNP Simulation

3.1.1 Single cell simulation (Source in the Cytoplasm)

The results of the absorbed dose calculations for the three radionuclides, Sr-90, I-131, and Cs-137 with the source located in the cytoplasm, are presented in Fig. 8. This figure shows that, beta dose deposition within the cellular components (1: Nucleus, 2: Cytoplasm, 3: Membrane) for Sr-90, I-131, and Cs-137 sources.

The similar trend observed for all three radionuclides indicates that the source position plays a significant role in the spatial distribution of the absorbed dose. As expected, because the source was located in the cytoplasm, this region received the highest dose values. In contrast, the cell membrane received the lowest dose due to its greater distance from the source as well as its smaller volume.

Additionally, the results indicated that Sr-90 produced the highest beta dose in the cytoplasm, whereas I-131 yielded the lowest dose in the cell membrane. Notably, although I-131 has higher maximum beta energy than the other two radionuclides, its local absorbed dose was the lowest. This behavior can be attributed to this fact that, as electron energy increases, the linear energy transfer (LET) decreases and the electron range increases. In other words, higher-energy electrons deposit less energy per unit path length and are more likely to escape the target region before depositing their all energies.

Furthermore, as shown in Figs. 8 and 9, the beta dose was approximately two orders of magnitude higher than the gamma dose, indicating the dominant contribution of beta particles to the cellular absorbed dose. This can be

Not Corrected Proof

attributed to the fact that only a small fraction of photon energy is absorbed within the target volume through Compton scattering and the generation of secondary electrons.

3.1.2 Single cell simulation (Source out of the cell)

When the source was located outside the cell, the dose distribution pattern among the cellular components changed. As the distance between the source and the cell increased, the particle flux decreased sharply, resulting in a corresponding reduction in the absorbed dose delivered to the cellular components. Under these conditions, the cell membrane received the highest dose because it was the closest compartment to the source. In this configuration, the membrane acts as the first barrier to beta particles. As a result, beta particles lose a significant portion of their energy while passing through the outer cell layer, causing the more internal components, namely the cytoplasm and nucleus, to receive lower doses.

When the source was positioned outside the cell, the gamma dose for both radionuclides increased slightly from the nucleus toward the cell membrane. Consequently, the membrane received the highest dose, while the nucleus received the minimum.

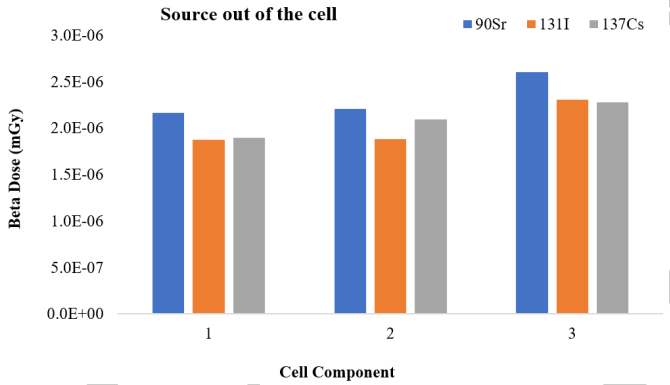

Figure 10: Beta dose deposition within the cellular components (1: Nucleus, 2: Cytoplasm, 3: Membrane) for Sr-90, I-131, and Cs-137 sources.

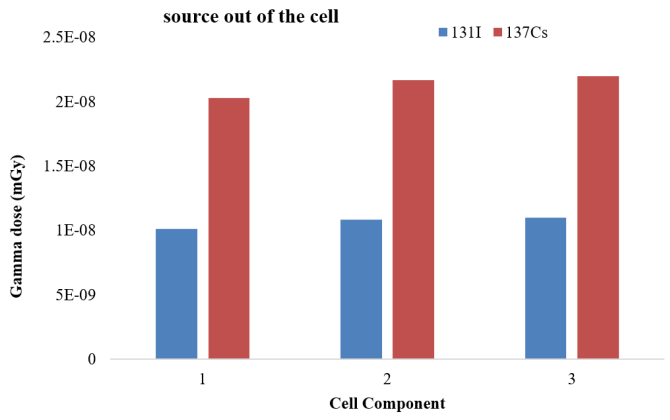

Figure 11: Gamma dose deposition within the cellular components (1: Nucleus, 2: Cytoplasm, 3: Membrane) for Sr-90, I-131, and Cs-137 sources.

3.1.3 Multi-cell simulation surrounding the central cell (Source in the middle of the nucleus)

In this case, according to the results, the highest absorbed dose was delivered to the central cell, whereas the dose received by the neighboring cells decreased significantly with increasing distance from the source.

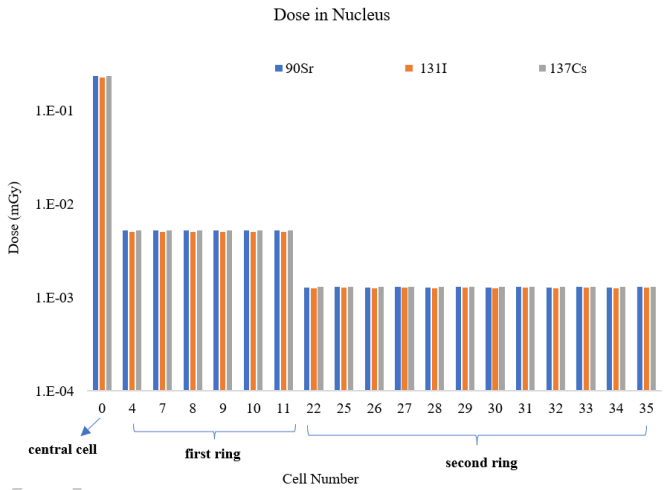

Figure 12: Beta dose deposition within the nucleus for Sr-90, I-131, and Cs-137 sources.

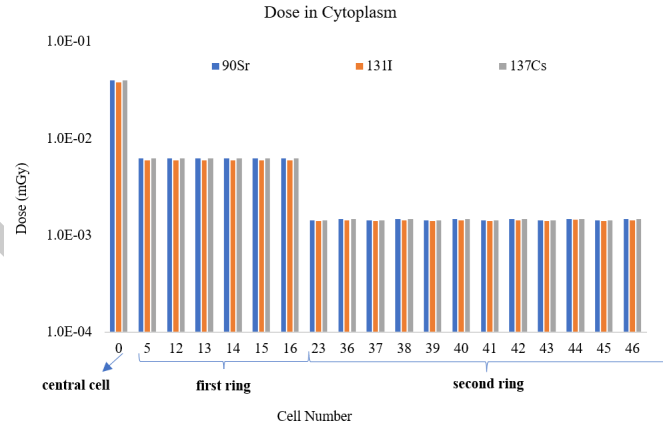

Figure 13: . Beta dose deposition within the cytoplasm for Sr-90, I-131, and Cs-137 sources.

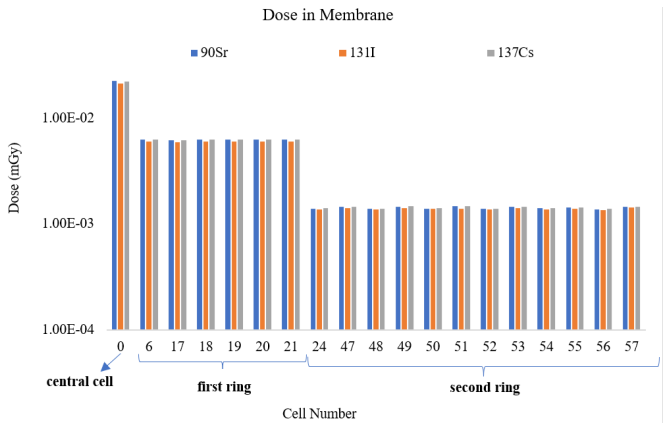

Figure 14: Beta dose deposition within the membrane for Sr-90, I-131, and Cs-137 sources.

The results show that the nucleus of the central cell received a considerably higher dose than the other cellular components. This can be attributed to the position of the source which leads to more localized energy deposition within the cell. The cells in the first and second rings (row) received substantially lower doses than the central cell; it is worth mentioning that the dose values within each of these two rings were highly uniform. As expected, this uniformity indicates that the cell arrangement geometry was relatively symmetrical and that the effective distance of each of these cells from the source was nearly identical.

The placement of the sources within the nucleus of the central cell creates a highly localized dose field, in which the nucleus of the source cell receives the greatest dose burden. Nevertheless, the surrounding cells also receive considerable doses, particularly those in the first ring. Therefore, although the maximum direct damage is concentrated in the source cell, biological responses may also be induced in neighboring cells. The sharp decrease in dose from the first to the second ring suggests that, the radiation effect has a limited cellular range and is largely confined to the immediate neighbors.

Overall, the results demonstrate that the highest dose was concentrated within the central cell, with the absorbed dose in all three cellular compartments decreasing significantly as the radial distance from the source increases. Furthermore, the dose distribution in the neighboring rings is relatively uniform.

The results for gamma dose distribution are demonstrated in Figs. 15 to 17.

Simulation results for dose distribution demonstrate that both I-131 and Cs-137 isotopes exhibit a similar trend of decreasing dose with increasing distance from the target cell. However, significant differences in energy deposition are evident. While both sources induce substantially higher doses in the central cell nucleus compared to peripheral cells, Cs-137 consistently delivers a higher dose across all cellular positions. This is primarily attributed to the higher gamma-photon energy of Cs-137 (662 keV) relative to the primary photons of I-131 (364 keV). The increased energy of Cs-137 enhances the probability of Compton scattering and photon penetration, thereby elevating the dose in adjacent nucleus.

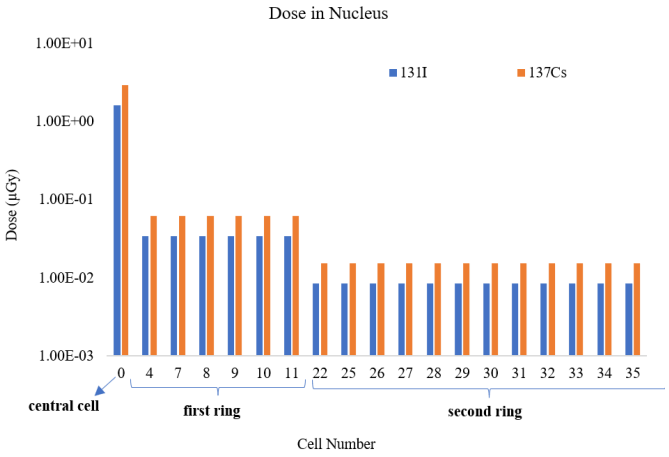

Figure 15: Gamma dose deposition within the nucleus for I-131 and Cs-137 sources.

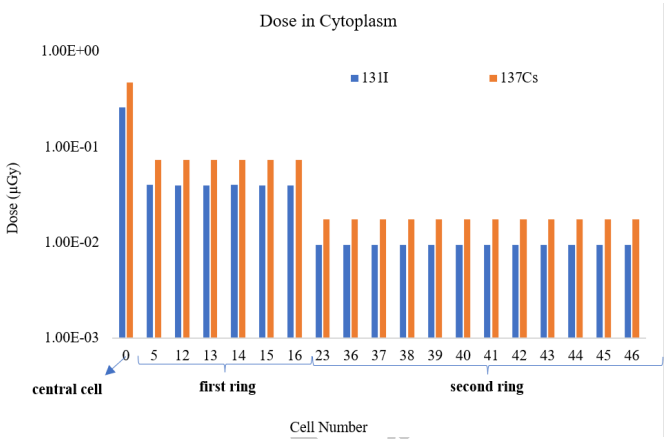

Figure 16: Gamma dose deposition within the cytoplasm for I-131 and Cs-137 sources.

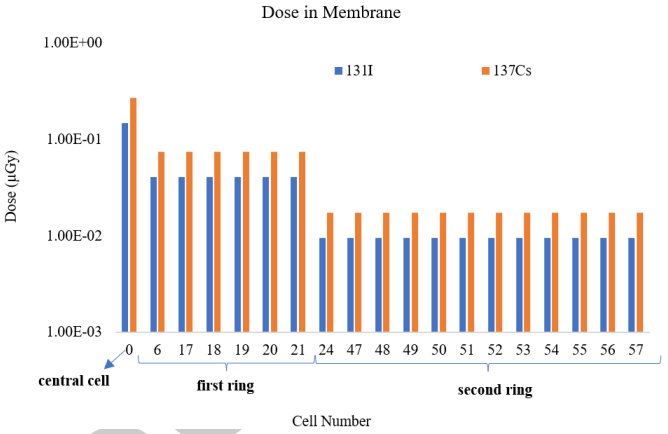

Figure 17: Gamma dose deposition within the membrane for I-131 and Cs-137 sources.

Regarding cytoplasmic dose distribution, both isotopes show a comparable declining trend as the distance from the source cell increases; however, the spatial dose distribution in the cytoplasm is more extensive than in the nucleus, a behavior attributable to the larger cytoplasmic volume. Specifically, Cs-137 generates a higher cytoplasmic dose than I-131, again due to superior photon penetration and increased Compton interaction probability. These findings underscore that, beyond nuclear dose, cytoplasmic energy deposition must be integrated into radiobiological assessments, given the significant role of this compartment in mediating indirect damage through oxidative stress and subcellular signaling pathways.

3.1.4 Multi cell simulation surrounding the central cell (Source in the cytoplasm)

The obtained results showed that when the beta sources were placed within the cytoplasm of the central cell, the dose distribution pattern depended strongly on the spatial location of the source, the limited range of electrons in the cellular environment, and the geometric arrangement of the neighboring cells. In this scenario, the highest dose was recorded in the cytoplasm of the central cell, which is fully consistent with physical expectations, since the region containing the source serves as the primary site of

Uncorrected Proof

interaction for the emitted particles and therefore receives the greatest deposited energy.

From a microdosimetric perspective, this finding is particularly important, as it demonstrates that even at the single- cell scale; displacement of the source from the nucleus to the cytoplasm can substantially alter the dose distribution pattern. In this case, a portion of the energy carried by the emitted electrons is deposited in the cytoplasm before the particles reach the nucleus. Consequently, although the nucleus still receives a considerable dose, it is no longer the dominant region in terms of deposited energy.

This observation is highly relevant to the analysis of biological damage, since the biological response depends not only on the total absorbed dose but also on the spatial distribution of energy deposition. Although the nucleus is generally regarded as the primary target for most genetic damage, high doses absorbed in the cytoplasm may also significantly influence the overall biological outcome through damage to organelles.

The corresponding beta- and gamma-dose distributions in the nucleus, cytoplasm, and cell membrane of the central and surrounding cells are presented in Figs. 18 to .23

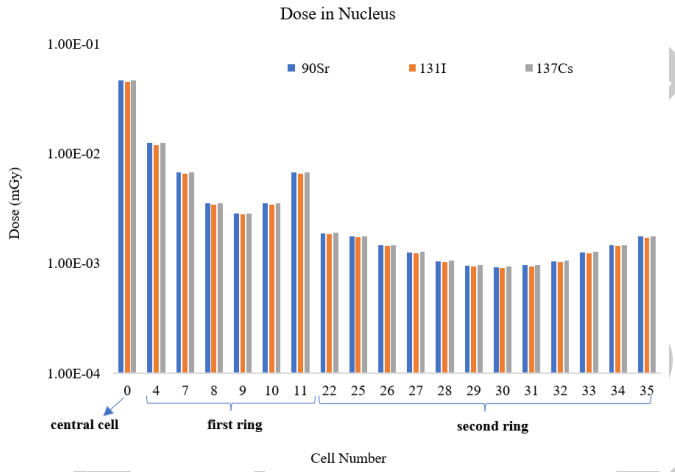

Figure 18: Beta dose deposition within the nucleus for Sr-90, I-131, and Cs-137 sources.

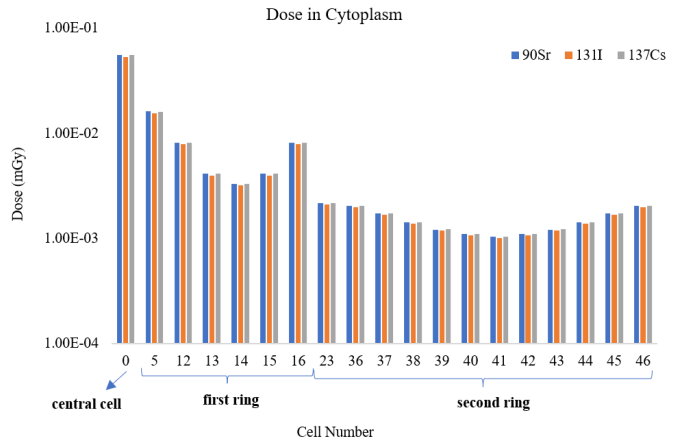

Figure 19: Beta dose deposition within the cytoplasm for Sr-90, I-131, and Cs-137 sources.

According to the above results, the gamma dose exhibits a decreasing trend with increasing distance from the source-containing cell. Similar to the previous results, the highest deposited dose is observed in the central cell, where the radionuclide is located within the cytoplasm, while the surrounding cells receive progressively lower doses. This behavior can be attributed to the attenuation of photon fluence and the reduction in interaction probability as the distance from the emission site increases.

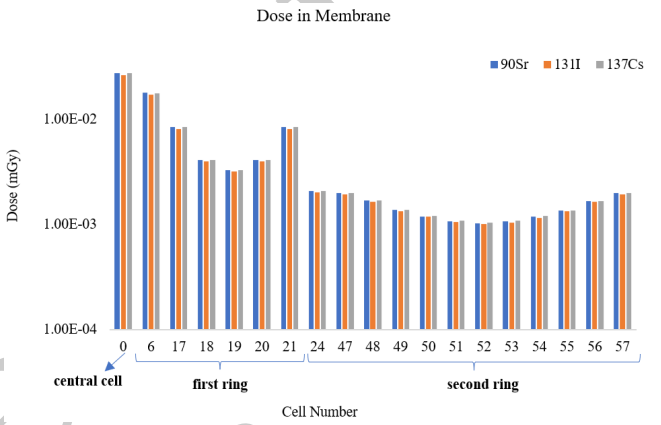

Figure 20: Beta dose deposition within the membrane for Sr-90, I-131, and Cs-137 sources.

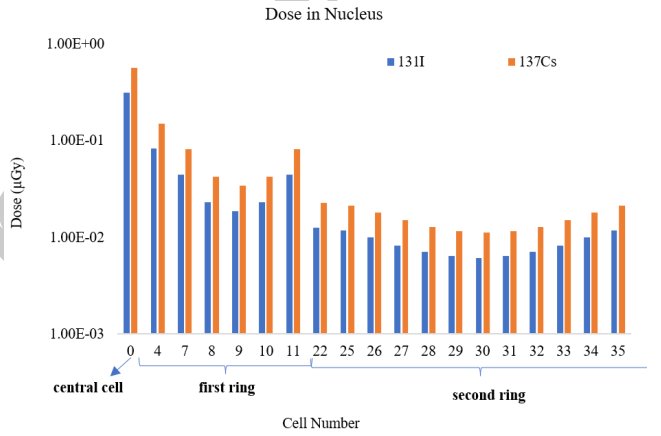

Figure 21: Gamma dose deposition within the nucleus for I-131 and Cs-137 sources.

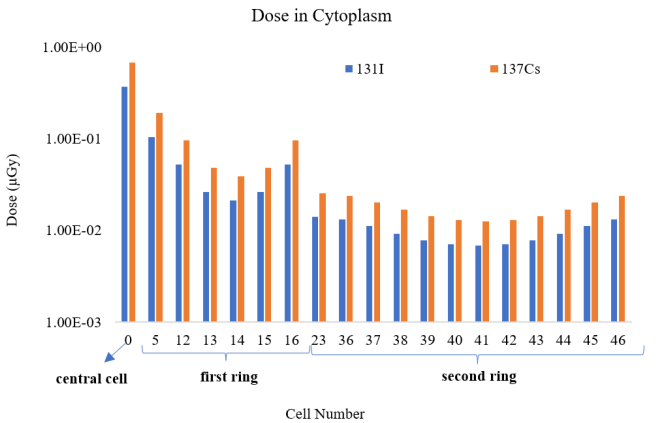

Figure 22: Gamma dose deposition within the cytoplasm for I-131 and Cs-137 sources.

Table 2: Calculated yields of DNA single-strand breaks (SSBs) and double-strand breaks (DSBs) for the investigated radionuclides.

Radionuclide	Radiation Type	SSB Yield ($Gy^{-1}.Gbp^{-1}$)	DSB Yield ($Gy^{-1}.Gbp^{-1}$)
Cs-137	γ (662 keV)	264.1 ± 1.3	3.5 ± 0.1
I-131	γ (364 keV)	88.5 ± 0.1	2.4 ± 0.2
I-131	β (606 keV)	278.9 ± 1.1	3.5 ± 0.1
Sr-90	β (2.38 MeV)	3.5 ± 1.9	0.85 ± 0.3
Sr-90	β (546 keV)	280.3 ± 16.7	3.5 ± 1.9
Moiseenko et al. (Moiseenko et al., 2001)	γ (662 keV)	81.1 ± 1.3	2.2 ± 0.2
Hsiao and Stewart (Hsiao and Stewart, 2008)	γ (662 keV)	188.3 ± 0.1	8.4 ± 0.1

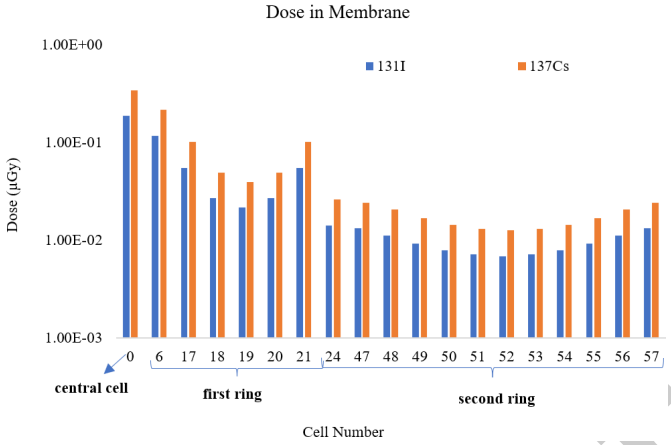

Figure 23: Gamma dose deposition within the membrane for I-131 and Cs-137 sources.

A comparison between the two gamma-emitting sources also indicates that Cs-137 produces a consistently higher dose than I-131 in both the central and neighboring cells. Similar to the previous results, this difference is mainly due to the higher gamma energy of Cs-137 (662 keV) compared with I-131 (364 keV), which enhances photon penetration and increases the contribution of Compton scattering in the surrounding cells. As a result, Cs-137 is able to transfer more energy not only to the source-containing cell but also to adjacent cells, leading to a broader and more pronounced dose distribution. Overall, the observed trend reflects the combined effects of source localization, photon energy, and spatial attenuation, which together govern the radial decrease of gamma dose in this model.

A qualitative comparison was made with previously published MCNP-based cellular dosimetry studies. Sadremomtaz and Masoumi (2018) investigated cellular dose distributions for several radionuclides and reported that the absorbed dose is strongly dependent on the source location within the cell, with the highest dose occurring in the compartment containing the source (Sadremomtaz and Masoumi, 2018). Similarly, Cai et al. (2010) demonstrated using MCNP that intracellular localization of the radionuclide leads to significantly higher nuclear doses compared with extracellular sources (Cai et al., 2010). Our single-cell results are consistent with these findings: when the source was placed in the cytoplasm, the highest beta dose was recorded in the cytoplasm, whereas an extracellular source resulted in the maximum dose being deposited in the cell membrane. Direct quantitative comparison, however, is limited due to differences in cell geometry, membrane thickness, radionuclide spectra, and scoring methods. Nevertheless, the overall trend regarding the critical influence of source position on cellular dose distribution is in good agreement with the existing MCNP literature.

3.2 Results of Geant4-DNA Simulation

The numbers of radiation-induced single-strand breaks (SSBs) and double-strand breaks (DSBs) obtained for the investigated radionuclides are summarized as follows. For Cs-137 gamma rays, the numbers of SSBs and DSBs were 52,925 ± 230 and 695 ± 26, respectively. For I-131 beta particles, the corresponding values were 64,956 ± 255 SSBs and 823 ± 29 DSBs. In the case of I-131 gamma rays, 7,238 ± 85 SSBs and 200 ± 14 DSBs were observed. For Sr-90 beta particles with an energy of 2.38 MeV, the numbers of SSBs and DSBs were 207 ± 14 and 5 ± 2, respectively, whereas for beta particles with an energy of 546 keV, the numbers increased to 66,730 ± 258 SSBs and 829 ± 29 DSBs.

The calculated yields of single-strand breaks (SSBs) and double-strand breaks (DSBs) are presented in Table 2. All uncertainties are reported with a coverage factor of $k = 1$, corresponding to a confidence level of approximately 68%. The obtained values were subsequently compared with those reported in previous studies, as discussed in Table 2. Furthermore, the yields obtained for Cs-137 gamma rays, reported by Moiseenko et al. (Moiseenko et al., 2001) and Hsiao and Stewart (Hsiao and Stewart, 2008), are presented in Table 2 to enable comparison of the simulation results.

The differences observed between the present results and those reported in previous studies can be attributed primarily to the DNA geometries and modeling approaches employed. Moiseenko et al. (Moiseenko et al., 2001) used a canonical B-DNA geometry consisting of 171 base pairs, whereas Hsiao and Stewart (Hsiao and Stewart, 2008) did not explicitly model the DNA structure. Instead, they simulated the cell and nucleus and estimated SSB and DSB yields based on the calculated probabilities of DNA damage occurrence. These differences in geometric representation and damage assessment methodology can significantly influence the predicted DNA damage yields.

The higher SSB and DSB yields obtained for 546 keV

Uncorrected Proof

beta particles compared with 2.38 MeV beta particles can be explained by their higher linear energy transfer (LET). Lower-energy beta particles deposit their energy more densely along their tracks, leading to a greater probability of inducing complex DNA damage and strand breaks. Consequently, the 546 keV beta particles exhibit a higher relative biological effectiveness than the more energetic 2.38 MeV beta particles.

4 Conclusion

In this study, the radiobiological effects of Cs-137, I-131, and Sr-90 were investigated using a combined Monte Carlo simulation framework based on MCNPX and Geant4-DNA. At the cellular level, the simulations demonstrated that the spatial location of the radionuclide source plays a critical role in determining the distribution of absorbed dose among the cellular compartments. When the source was located within the cytoplasm, the highest dose was deposited in the cytoplasm of the source-containing cell, whereas an extracellular source resulted in the highest dose being deposited in the cell membrane. These findings highlight the importance of source localization in cellular dosimetry, particularly for radionuclides that may accumulate within specific tissues or cellular compartments.

The multicellular simulations further demonstrated that the absorbed dose was strongly concentrated in the source-containing cell and decreased with increasing distance from the source. Although the central cell received the highest dose, measurable doses were also deposited in neighboring cells, particularly those located in the first surrounding ring. The relatively uniform dose distribution within each ring was consistent with the symmetrical arrangement of the cells. These results indicate that the spatial distribution of radiation dose at the multicellular scale should be considered when evaluating the potential biological effects of localized radionuclide contamination.

The comparison of beta-emitting radionuclides showed that lower-energy beta particles produced greater localized energy deposition and higher DNA damage yields than higher-energy beta particles. In particular, the 546 keV beta particles emitted in the Sr-90 decay system produced substantially higher SSB and DSB yields than the 2.38 MeV beta particles. This behavior is consistent with the greater localized energy deposition associated with lower-energy electrons. For the gamma-emitting radionuclides, Cs-137 produced higher cellular doses than I-131 in the present multicellular configuration, reflecting the greater penetrating capability of its 662 keV gamma photons compared with the 364 keV photons of I-131.

At the molecular level, the Geant4-DNA simulations demonstrated clear differences in DNA strand-break induction among the investigated radiation types. The calculated SSB and DSB yields showed that radiation quality and electron energy strongly influence the pattern and magnitude of DNA damage. The obtained values were in reasonable agreement with previously published results, while the observed differences can be attributed mainly to variations in DNA geometry, source definition, and damage-assessment methodology.

Overall, the combined use of MCNPX and Geant4-DNA provides a useful multiscale framework that links radionuclide-specific radiation transport and cellular dose distributions to nanoscale DNA damage.The results emphasize that absorbed dose alone may not fully describe the potential biological impact of radionuclide exposure, since the radiation type, source localization, energy deposition pattern, and spatial distribution of dose can substantially affect the resulting biological damage. This computational framework can therefore contribute to a more detailed assessment of radiobiological effects and may provide useful insights for radiation protection and risk assessment in scenarios involving accidental radionuclide releases.

Conflict of Interest

The authors declare no potential conflict of interest regarding the publication of this work.

Funding

The authors declare that no funds, grants, or other financial support were received during the preparation of this manuscript.

References

Agostinelli, S. et al. (2003). GEANT4-a simulation toolkit. *Nuclear Instruments and Methods in Physics Research Section A: Accelerators, Spectrometers, Detectors and Associated Equipment*, 506(3):250–303.

Cai, Z., Pignol, J. P., Chan, C., et al. (2010). Cellular dosimetry of ^{111}In using Monte Carlo N-Particle computer code: comparison with analytic methods and correlation with in vitro cytotoxicity. *Journal of Nuclear Medicine*, 51(3):462–470.

Chino, M., Nakayama, H., Nagai, H., et al. (2011). Preliminary estimation of release amounts of ^{131}I and ^{137}Cs accidentally discharged from the Fukushima Daiichi nuclear power plant into the atmosphere. *Journal of Nuclear Science and Technology*, 48(7):1129–1134.

de la Fuente Rosales, L., Incerti, S., Francis, Z., et al. (2018). Accounting for radiation-induced indirect damage on DNA with the Geant4-DNA code. *Physica Medica*, 51:108–116.

El Naqa, I., Pater, P., and Seuntjens, J. (2012). Monte Carlo role in radiobiological modelling of radiotherapy outcomes. *Physics in Medicine and Biology*, 57(11):R75–R97.

Hada, M. and Georgakilas, A. G. (2008). Formation of clustered DNA damage after high-LET irradiation: a review. *Journal of Radiation Research*, 49(3):203–210.

Higley, K. A. (2006). Environmental consequences of the Chernobyl accident and their remediation: twenty years of experience. report of the Chernobyl forum expert group 'Environment' STI/PUB/1239, 2006, International Atomic Energy Agency, Vienna, Austria ISBN: 92-0-114705-8, 166 pp, 40.00 Euros (softbound). *Radiation Protection Dosimetry*, 121(4):476–477.

Uncorrected Proof

Hsiao, Y. and Stewart, R. D. (2008). Monte Carlo simulation of DNA damage induction by X-rays and selected radioisotopes. *Physics in Medicine and Biology*, 53:233–244.

IAEA (2015). Response for a nuclear or radiological emergency. *Vienna, Austria: International Atomic Energy Agency*.

IAEA (n.d.). *Radiation Biology: A Handbook for Teachers and Students*. International Atomic Energy Agency.

Jolly, A. L. and Fielding, A. L. (2025). Modelling single cell dosimetry and DNA damage of targeted alpha therapy using Monte-Carlo techniques. *Physical and Engineering Sciences in Medicine*, 48(4):1611–1624.

Kocher, D. C. (1980). Radioactive decay data tables. Technical Report DOE/TIC-11026, Oak Ridge National Lab., TN (USA).

Kyriakou, I., Sakata, D., Tran, H. N., et al. (2021). Review of the Geant4-DNA simulation toolkit for radiobiological applications at the cellular and DNA level. *Cancers*, 14(1):35.

Leblond, S. (2024). DDEP re-evaluation of the radioactive decay scheme of ^{137}Cs. *Applied Radiation and Isotopes*, 206:111191.

Mészáros, R., Leelőssy, Á., Kovács, T., et al. (2016). Predictability of the dispersion of Fukushima-derived radionuclides and their homogenization in the atmosphere. *Scientific Reports*, 6(1):19915.

Moiseenko, V. V. et al. (2001). Calculation of radiation-induced DNA damage from photons and tritium beta particles, Part 1: Model formulation and basic results. *Radiation and Environmental Biophysics*, 40:23–31.

Nam, J. S., Choi, Y. S., Hong, S. B., et al. (2017). Study on the characteristics of a scintillator for Beta-ray detection using epoxy resin. In *EPJ Web of Conferences*, volume 153, page 07005. EDP Sciences.

National Research Council (2006). BEIR VII report: Health risks from exposure to low levels of ionizing radiation. Technical report, The National Academies Press.

Nikjoo, H., O'Neill, P., Goodhead, D. T., et al. (1997). Computational modelling of low-energy electron-induced DNA damage by early physical and chemical events. *International Journal of Radiation Biology*, 71(5):467–483.

Ory, C., Leboulleux, S., Salvatore, D., et al. (2021). Consequences of atmospheric contamination by radioiodine: the Chernobyl and Fukushima accidents. *Endocrine*, 71(2):298–309.

Paquet, F., Bailey, M. R., Leggett, R. W., et al. (2017). ICRP publication 137: occupational intakes of radionuclides: part 3. *Annals of the ICRP*, 46(3-4):1–486.

Sadremomtaz, A. and Masoumi, M. (2018). Cellular dosimetry of different radionuclides for targeted radionuclide therapy: Monte Carlo simulation. *Biomedical Physics & Engineering Express*, 4(6):065006.

Sakata, D., Belov, O., Bordage, M. C., et al. (2020). Fully integrated Monte Carlo simulation for evaluating radiation induced DNA damage and subsequent repair using Geant4-DNA. *Scientific Reports*, 10(1):20788.

Semsarha, F. et al. (2014). An investigation on the radiation sensitivity of DNA conformations to ^{60}Co gamma rays by using Geant4 toolkit. *Nuclear Instruments and Methods in Physics Research Section B: Beam Interaction with Materials and Atoms*, 323:75–78.

Steinhauser, G., Brandl, A., and Johnson, T. E. (2014). Comparison of the Chernobyl and Fukushima nuclear accidents: a review of the environmental impacts. *Science of the Total Environment*, 470:800–817.

Taylor, B. N. (2009). *Guidelines for Evaluation and Expressing the Uncertainty of NIST Measurement Results*. DIANE Publishing.

United Nations Scientific Committee on the Effects of Atomic Radiation (2021). Sources, effects and risks of ionizing radiation: UNSCEAR 2020/2021 report to the general assembly, with scientific annexes. Technical report, United Nations.

UNSCEAR (2021). UNSCEAR 2020/2021 Fukushima reports. Technical report, United Nations Scientific Committee on the Effects of Atomic Radiation.

Wai, K. M., Krstic, D., Nikezic, D., et al. (2020). External Cesium-137 doses to humans from soil influenced by the Fukushima and Chernobyl nuclear power plants accidents: a comparative study. *Scientific Reports*, 10(1):7902.

Uncorrected Proof

©2027 by the journal.

RPE is licensed under a Creative Commons Attribution-NonCommercial 4.0 International License (CC BY-NC 4.0).





To cite this article:

K. Kangarlou, B. Jalali Kondori, M. T. Holisaz, P. Taghipour Niyar, M. Soleimaninia, A. Moslehi, A. Mosayebi, S. P. Shirmardi, S. M. Mazidi Linking cellular dosimetry and nanoscale DNA damage of key accident radionuclides using MCNPX and Geant4-DNA . *Radiation Physics and Engineering*, In Press.

DOI:

To link to this article: